

High-Temperature Stable Gold Nanoparticle Catalysts for Application under Severe Conditions: The Role of TiO₂ Nanodomains in Structure and Activity

Begoña Puértolas,[†] Álvaro Mayoral,[‡] Raul Arenal,^{‡,§} Benjamín Solsona,^{*,#} Alaina Moragues,[‡] Sonia Murcia-Mascaros,[‡] Pedro Amorós,[‡] Ana B. Hungría,^Δ Stuart H. Taylor,[○] and Tomás García^{*,†}

[†]Instituto de Carboquímica (ICB-CSIC), C/ Miguel Luesma Castán 4, 50018 Zaragoza, Spain

[‡]Laboratorio de Microscopias Avanzadas (LMA), Instituto de Nanociencia de Aragon (INA), Universidad de Zaragoza, Mariano Esquillor, 50018 Zaragoza, Spain

[§]Fundación Agencia Aragonesa para la Investigación y el Desarrollo (ARAID), María de Luna 11, 50018 Zaragoza, Spain

[#]Departamento de Ingeniería Química, Universitat de València, Avinguda de la Universitat s/n, 46100 Burjassot, Spain

^ΔInstituto de Ciencia de los Materiales, Universitat de València, P.O. Box 22085, 46071 Valencia, Spain

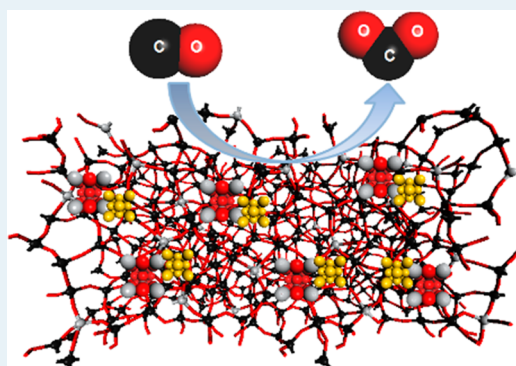
[○]Departamento de Ciencia de Materiales, Ingeniería Metalúrgica y Química Inorgánica, Universidad de Cádiz, Campus Río San Pedro, 11510 Puerto Real, Spain

[○]Cardiff Catalysis Institute, School of Chemistry, Cardiff University, Main Building, Park Place, CF10 3AT Cardiff, United Kingdom

Supporting Information

ABSTRACT: Metal nanoparticles with precisely controlled size are highly attractive for heterogeneous catalysis. However, their poor thermal stability remains a major concern in their application at realistic operating conditions. This paper demonstrates the possibility of synthesizing gold nanoparticles with exceptional thermal stability. This has been achieved by using a simple conventional deposition–precipitation technique. The material employed as catalyst consists of gold supported on a TiO₂-impregnated SiO₂ bimodal mesoporous support. The resulting material shows gold nanoparticles with a narrow size distribution around 3.0 nm, homogeneously dispersed over the TiO₂/SiO₂ material. Most interestingly, the gold nanoparticles show exceptional thermal stability; calcination temperatures as high as 800 °C have been employed, and negligible changes in the gold particle size distribution are apparent. Additionally, the presence of an amorphous titanium silicate phase is partially preserved, and these factors lead to remarkable activity to catalyze a range of oxidation reactions.

KEYWORDS: heterogeneous catalysis, gold nanoparticles, stability, mesoporous materials, catalytic oxidation



The nature and properties of catalysts based on gold nanoparticles dispersed on oxide supports have received much recent attention,^{1,2} due to their high activity in many industrially and environmentally important reactions. Especially significant is the capacity of subnanometer gold to oxidize CO to CO₂ at very low temperatures.^{3,4} To date, the most active gold catalysts for CO oxidation are generally supported on reducible metal oxides, such as TiO₂ or Fe₂O₃, which are either uncalcined or calcined at temperatures <500 °C.^{5–7} The discovery of gold-based catalysts showing exceptional low-temperature CO oxidation activity resulted in an explosion of interest into these types of catalysts, and they have now been successfully applied to catalyze a wide range of reactions. However, an inherent problem for nanoparticulate catalysts is their well-documented lack of thermal stability under highly demanding operating conditions.^{8–10} Supported and unsupported metal nanoparticles show rapid particle aggregation,

especially at elevated reaction temperatures.^{8,9} For many industrially important catalytic applications, reaction temperatures typically exceed 600 °C, and hydrothermal stability of the catalysts becomes a crucial issue.^{11,12} Indeed, the development of heat-stable Au-based catalysts represents a true challenge and will offer new opportunities for Au nanoparticle catalysis if innovative routes to Au nanoparticle stabilization at high temperatures are proposed. Strategies such as post modification of Au/TiO₂ by amorphous SiO₂ decoration,¹³ the production of core–shell nanostructures,^{14–16} FeO_x-modified hydroxyapatite supported gold catalysts,¹⁷ or the synthesis of thin porous alumina sheets¹⁸ have been adopted to

Received: November 5, 2014

Revised: December 26, 2014

Published: January 6, 2015

address this problem. These strategies certainly reduce the tendency to sinter at high temperatures. However, they have limitations, as they can use expensive precursors or highly complex synthesis procedures.

One of the main areas of opportunity concerns the automotive industry, where low-temperature start-up performance of catalysts remains an area in which improvement is sought. The most widespread technologies of hybrid vehicles or micro hybrid cars (start–stop systems) require the development of efficient catalytic systems for the control of vehicle exhaust emissions during this period. Moreover, in addition to the promising technical performance afforded by gold-based catalysts, the relatively stable lower price and greater availability of gold compared with the platinum group metals remain excellent economic reasons for pursuing the development of pollution control technologies based on this metal.¹⁹ In this respect, there is a desire to be able to prepare gold nanoparticulate catalysts that have increased stability at high temperatures, as this will significantly extend the application of these catalysts for new processes.

Herein, we demonstrate the possibility of synthesizing gold nanoparticles with exceptional thermal stability. The material employed as a catalyst consists of gold nanoparticles supported on a UVM-7 nanoparticulate bimodal mesoporous material,^{20–22} which has first been modified by impregnation to form TiO₂ domains. The resulting material shows gold nanoparticles with a narrow size distribution around 3.0 nm, homogeneously dispersed over the TiO₂/SiO₂ material; the nanoparticle sizes do not increase after calcination at temperatures as high as 800 °C. To the best of our knowledge, such a result has not been reported previously.

■ EXPERIMENTAL SECTION

Materials. The synthesis of UVM-7 was based on the “atrane route” with a molar composition of 2TEOS–7TEAH3–0.52CTMABr–180H₂O.²⁰ In a typical synthesis, the corresponding amounts of TEOS (Fluka 98%) and TEAH3 (Sigma-Aldrich ≥ 99%) were mixed under continuous stirring at 140 °C until a homogeneous dispersion was achieved. Then, the temperature was decreased to 120 °C, and the CTMABr (Sigma-Aldrich 98%) was added. The resulting gel was cooled to 80 °C when distilled water was added. This mixture was allowed to age at room temperature overnight under continuous stirring. The resulting mesostructured powder was separated by filtration, washed extensively with deionized water and ethanol, and dried at 60 °C overnight. To prepare the final porous material, the template was removed by calcination at 550 °C for 6 h (heating ramp = 5 °C/min) under static air atmosphere.

Different metal oxides were incorporated into the UVM-7 support: TiO₂, ZrO₂, and CeO₂–ZrO₂. Although we used a similar impregnation strategy regardless of the different metal oxides included inside the UVM-7 mesopores, some experimental details have been optimized depending on the chemical nature of the reagent used.

TiO₂/UVM-7 was synthesized by a post-synthetic wet impregnation procedure previously described by Narkhede et al.²³ Four different titania loadings were tested: from Ti/(Ti + Si) of 3–40 wt %. To achieve these loadings, the corresponding weight of TiO(acac)₂ (Sigma-Aldrich 90%) was taken in 100 cm³ of pure ethanol (Scharlau, HPLC grade). Then, deionized water was slowly added with continuous vigorous stirring. Subsequently, the impregnation of the

calcined UVM-7 silica support (0.6 g) was carried out by stirring the sample for 2 h with the Ti solution. The mixture was filtered and washed thoroughly. The cake was allowed to dry overnight at room temperature, and the TiO₂/UVM-7 was calcined in air at 300 °C for 5 h with a heating rate of 1 °C/min.

ZrO₂/UVM-7 was synthesized by a conventional wet impregnation procedure. ZrO(NO₃)₂·xH₂O (1.83 g; Sigma-Aldrich, technical grade) was dissolved in 30 cm³ of deionized water under vigorous stirring. Impregnation of the calcined UVM-7 silica support (0.6 g) was carried out by stirring the sample for 13 h with the Zr solution. The mixture was allowed to dry overnight at 110 °C, and the resulting ZrO₂/UVM-7 was calcined in air at 550 °C for 4 h with a heating rate of 1 °C/min. The Zr loading was 54.6 wt %.

CeO₂–ZrO₂/UVM-7 was also synthesized by a conventional wet impregnation procedure. ZrO(NO₃)₂·xH₂O (0.91 g) and 1.42 g of Ce(NO₃)₃·6H₂O (Sigma-Aldrich 99%) were dissolved in 30 cm³ of deionized water under vigorous stirring. Impregnation of the calcined UVM-7 silica support (0.6 g) was carried out by stirring the sample for 13 h with the Ce–Zr solution. The mixture was allowed to dry overnight at 110 °C and the CeO₂–ZrO₂/UVM-7 was calcined in air at 550 °C for 4 h with a heating rate of 1 °C/min. The cerium and zirconium loadings were 37.6 and 43.3 wt %, respectively. Compared to TiO₂, in which relatively soft thermal conditions were used to favor first the melting of the TiO(acac)₂ and later its thermal evolution to oxide, in the case of Zr and Ce derivatives different calcination conditions were employed to promote the evolution of nitrates and oxide formation.

The gold incorporation onto the TiO₂/UVM-7, ZrO₂/UVM-7, and CeO₂–ZrO₂/UVM-7 matrices was carried out by the conventional deposition–precipitation technique. An aqueous solution (43.4 cm³; 5.078 × 10^{−3} M) of KAuCl₄ (Sigma-Aldrich 98%) was heated in a water bath wrapped with aluminum foil to exclude light at 70 °C. The initial pH was around 2.5. It was carefully adjusted to neutral pH by dropwise addition of a 0.1 M aqueous solution of NaOH (Sigma-Aldrich ≥ 98%). The pH was maintained around 7 for 30 min. Half a gram of the required UVM-7 support was then added, and pH excursions into the acidic region were controlled by adding NaOH. After the pH was constant for 15 min, the suspension was stirred for another hour at the same temperature. Finally, the suspension was cooled, filtered, and washed with deionized water. The resulting cake was heated at 90 °C for 13 h. After the preparation, the samples were stored in the dark in a vacuum desiccator at room temperature. Each sample was divided into three portions: the first portion was kept uncalcined; the second portion was calcined at 400 °C in static air for 4 h with a heating rate of 1 °C/min; and the third portion was calcined at 800 °C in static air under the same conditions. In all cases, the final catalysts were stored in a vacuum desiccator at room temperature.

Characterization. For electron microscopy analyses, the samples were dispersed in ethanol and placed onto a carbon-coated copper microgrid and left to dry before observation. Spherical aberration (C_s) corrected scanning transmission electron microscopy high-angle annular field (STEM-HAADF) imaging analyses were performed in a XFEG FEI Titan microscope operated at 300 kV. The microscope was equipped with a CEOS aberration corrector for the electron probe, achieving a point resolution of 0.8 Å, an EDAX EDS detector, and Gatan Energy Filter Tridiem HR865 for electron

energy loss spectroscopy (EELS). These spectroscopic data were obtained using the spectrum-image acquisition mode.^{24,25}

X-ray photoelectron spectroscopy (XPS) measurements were made on an Omicron ESCA+ photoelectron spectrometer using a nonmonochromatized Mg K α X-ray source ($h\nu = 1253.6$ eV). An analyzer pass energy of 50 eV was used for survey scans and 20 eV for detailed scans. Binding energies were referenced to the C1s peak from adventitious carbonaceous contamination, assumed to have a binding energy of 284.5 eV.

Powder X-ray diffraction (XRD) was carried out using a Bruker D8 Advance diffractometer with monochromatic Cu K α source operated at 40 kV and 40 mA.

The textural characterization of the samples was carried out by N₂ adsorption at -196 °C, using a Micromeritics ASAP 2020 apparatus. Prior to the adsorption measurements, the samples were outgassed in situ in vacuum at 250 °C for 4 h to remove adsorbed gases. Surface areas were calculated from nitrogen adsorption isotherms in the relative pressure range from 0.1 to 0.25 using the BET equation (S_{BET}). Both BJH pore size distributions and volumes were obtained from the adsorption branch of the N₂ adsorption isotherms. In addition, specific surface area, and total intraparticle pore volume (micro- and mesopore) were also estimated using the nonlocalized density functional theory (NLDFT) method. The model used for the NLDFT evaluation was N₂ adsorbed on silica with cylindrical pores, considering the adsorption branch of the isotherm.

Raman spectra were obtained using a HORIBA Jobin Yvon iHR320 spectrometer with Peltier-cooled CCD and a 532 and 785 nm doubled YAG laser as excitation.

²⁹Si MAS NMR spectra were recorded on a Varian Unity 300 spectrometer operating at 79.5 MHz and using a magic angle spinning speed of at least 4.0 kHz.

The gold loading was determined by energy dispersive X-ray spectroscopy EDX analysis using a scanning electron microscope (Philips SEM-XL 30).

Catalytic Testing. CO catalytic oxidation was performed at atmospheric pressure and at a temperature of 20 °C, using a fixed-bed reactor with an inner diameter of 5.8 mm. A mixture of 0.4% v/v CO, 20% v/v O₂, and argon balance was passed over 10 mg of catalyst with a flow rate of 100 cm³/min, which corresponded to a space velocity of 600000 cm³/(g_{cat}·h). Analyses were performed by an online gas chromatograph (Varian CP-3800) with thermal conductivity, and the conversion of CO and the formation of CO₂ were both quantified, which led us to measure a carbon balance with an accuracy of $\pm 2\%$. After being used in the reactor, the catalysts were stored at room temperature in a vacuum desiccator before spectroscopic analysis.

The Au/Ti8/UVM-7 800 catalyst performance was tested under simulated cold-start conditions by means of cold-start tests (CST). CST experiments were carried out in a fixed-bed reactor (diameter = 0.457 cm) under conditions that closely resembled the automotive “cold-start”. In the course of the simulated CSTs, the reactor temperature was increased from 30 to 600 °C at 50 °C/min, and held at this temperature for a further 30 min. The temperature was measured by a thermocouple located at the top of the catalyst bed. The inlet gas composition used for CST experiments was 1.6% v/v CO, 0.01% v/v propene, 0.0087% v/v toluene, 1% v/v oxygen, and 10% v/v water in argon, leading to a total flow of 100 cm³ STP/min and a gas hourly space velocity (GHSV) of 200000 h⁻¹.

Aliquots of the outlet stream were analyzed online using a quadrupole spectrometer (Omnistar, Pfeiffer vacuum). The following masses were monitored: m/z 40 for argon, m/z 28 for CO, m/z 42 for propene, m/z 91 for toluene, m/z 32 for oxygen, and m/z 18 for water; m/z 44 related to CO₂ formation was also followed during the experiment. Finally, 10 consecutive CSTs were performed once the reactor was cooled to assess the reusability and stability of the catalyst. Carbon balances were closed in all of the experiments ($100 \pm 3\%$).

Moreover, to evaluate the hydrothermal stability of the Au/Ti8/UVM-7 800 catalyst and its performance as a three-way catalyst, three consecutive cycles were performed under a gas flow that simulated the real exhaust gases of a diesel engine. The inlet gas composition used in the experiments was 1% v/v CO, 0.1% v/v propane, 0.03% v/v NO, 8% v/v O₂, 6% v/v CO₂, 8% v/v H₂O, and nitrogen balance under a total flow of 200 cm³/min. Flow rates of all gases were controlled by mass flow controllers. The experiments were run in a fixed-bed reactor (GHSV = 40000 h⁻¹) externally heated and coupled to an infrared spectrometer (Gaset DX4000). Carbon balances were closed in all of the experiments with an accuracy of $\pm 3\%$.

The Au/Ti8/UVM-7 800 catalyst performance was also tested for methane combustion. The activity test for catalytic methane oxidation was conducted in a fixed-bed reactor under isothermal conditions. One percent v/v CH₄ in air was flowed by mass flow controllers at a space velocity of 60000 h⁻¹. Analyses were performed by an online gas chromatograph (Varian CP-3800) with thermal conductivity and flame ionization detectors, and the conversion of CH₄ and the formation of CO₂ were both quantified, giving a carbon balance with an accuracy of $\pm 2\%$.

RESULTS AND DISCUSSION

The mesoporous silica UVM-7 is loaded with four different concentrations of TiO₂ to achieve Ti/(Ti + Si) ratios of 3, 8, 15, and 40 wt %. The preparation method is based on a simple wet impregnation of UVM-7 with titanium(IV) oxyacetylacetonate (TiO(acac)₂) calcining the samples at 300 °C with a very slow heating ramp, and the conventional deposition–precipitation technique is employed for the addition of gold onto the mesoporous TiO₂/UVM-7 matrix. The use of a slow heating ramp is crucial to obtain beneficial dispersion of the titanium species. The TiO(acac)₂ melts at ca. 200 °C, which is below the temperature of complex degradation, and leads to a homogeneous dispersion of Ti species over the internal surface of the UVM-7 silica. After gold deposition, several catalysts were prepared by heating the samples in air at temperatures of 400 and 800 °C, and comparison was made with a sample that was dried, but not calcined at high temperature. The samples are coded Au/TiX/UVM-7 CT, where X and CT represent the titania loading (3, 8, 15, and 40 wt %) and the calcination temperature (400 or 800 °C), respectively. Gold loadings of representative uncalcined and calcined catalysts are compiled in Table S1 in the Supporting Information and range from 2 to 5 wt % depending on titania loading. Additionally, a slightly higher gold loading is observed in the uncalcined samples. Experimental error in the determination of the gold content (± 0.2 wt %) can have an influence on these differences. However, it cannot be completely discarded that the marginal evaporation of large gold particles into the gas phase followed by the treatment at high temperatures²⁶ could be taking place. The simplicity of the preparation method as well as ease of

Table 1. Comparison of the CO Oxidation Activity of the UVM-7-Based Catalysts with Those of Other Catalysts Reported in the Literature

support	gold content ^a (wt %)	catalytic performance	T_{cal}^b (°C)	D_{Au}^c (nm)	space velocity (cm ³ /(g _{cat} ·h))	mol CO/(g _{cat} ·h)·(10 ³) at 20 °C	ref
TiO ₂ /SiO ₂	2.2	$T_{50} = 64$ °C	700	6.5	44000	9.0 at 64 °C	13
ZrO ₂		$T_{50} = 200$ °C	800	15	80000	2.3	14
TiO ₂ /Si-Al ₂ O ₃	1	$T_{50} = 50$ °C	600	3.0	36000	6.0 at 30 °C	15
FeO _x	3.2	$T_{50} = 22$ °C	600	4.5	20000	3.6	17
AlO _x	3.0	$T_{50} = -3$ °C	700	2.2	80000	30.0	18
AlO _x	3.0	$T_{50} = -3$ °C	900	2.2	80000	2.6	18
TiO ₂ /UVM-7	2.1	$X_{\text{CO}}^d = 15\%$	800	3.5 ± 1.6	600000	17.5	this study
ZrO ₂ /UVM-7	5.7	$X_{\text{CO}} = 45\%$	800	8.7 ± 3.9	25000	2.6	this study
CeO ₂ -ZrO ₂ /UVM-7	3.2	$X_{\text{CO}} = 72\%$	800	6.4 ± 2.6	35000	6.1	this study

^aThe gold loading (wt %) in our catalysts is determined by EDX. ^b T_{cal} , calcination temperature (°C) ^cThe gold mean particle size in our catalysts is determined by TEM. Conditions: 0.4% v/v CO, 20% v/v O₂ and argon balance, reaction temperature = 20 °C. ^d X_{CO} , CO conversion for the CO oxidation reaction.

scale-up are major advantages from the perspective of application.

Ambient temperature CO oxidation was used as an initial model reaction to probe the catalysts performance (Figures S1 and S2). The optimal titanium loading is 8 wt % (Figure S1 and Table S2). Increasing the calcination temperature of the catalysts leads to a decrease of the CO conversion, but the catalyst stability increases (Figure S2). Following calcination at 400 and 800 °C there is no deactivation over the test period, whereas for the uncalcined catalyst, conversion is not stable as the catalytic activity slightly decreases with time online. It is noteworthy that in addition to the excellent stability, the catalyst calcined at 800 °C still presents very high activity, as test conditions employ a very short contact time. Table 1 shows comparative CO oxidation results from the literature for gold-based catalysts heat treated at ≥ 600 °C. Our Au/Ti8/UVM-7 800 catalyst oxidizes CO at 20 °C using a high space velocity of 600000 cm³/(g_{cat}·h), with a CO conversion rate of 0.0175 mol CO/(g_{cat}·h), which is, to the best of our knowledge, the highest activity currently reported in the literature for gold catalysts calcined at high temperature.

A wide variety of different silica supports are available, but we specifically select UVM-7 due to its open framework and enhanced accessibility, as a consequence of hierarchic porosity with large interparticle voids and 3D interconnected short-length (ca. 25–30 nm) nanometric mesopores of ca. 3 nm (when CTABr is used as template). These characteristics, which are not present in other silicas such as MCM-41, MCM-48, or SBA-15 (usually obtained as large micrometric particles with unimodal long-length mesopores), favor mass diffusion throughout the hierarchic pore structure.²² This aspect could be beneficial, both at the preparative level, as a very homogeneous dispersion of both titanium and gold nanoparticles can be achieved, favoring the impregnation with the TiO(acac)₂ and KAuCl₄ solutions, and also for accessibility to active sites of the catalyst during operation. Accordingly, this catalytic system both uncalcined and calcined at conventional temperature (400 °C) also shows higher catalytic activity than a commercial gold/TiO₂-based catalyst supplied by the World Gold Council (Table S2). Therefore, an outstanding activity and stability is obtained for this material, which is even more noteworthy considering it is calcined at the high temperature of 800 °C. In contrast to that observed for Au/TiO₂/UVM-7 800 catalyst, the heat treatment of the Au/TiO₂ catalyst supplied by the World Gold Council at 800 °C led to a severe deactivation of the

catalyst, which exhibited a productivity ca. 600 times lower than that observed for Au/Ti8/UVM-7 800. A sintering of the gold particles takes place, and most of the gold crystallites are in the 12–20 nm range.

The remarkable performance of this catalytic system can be related first to the presence of small gold nanoparticles, which are resistant to sintering. Panels a and b of Figure 1 show

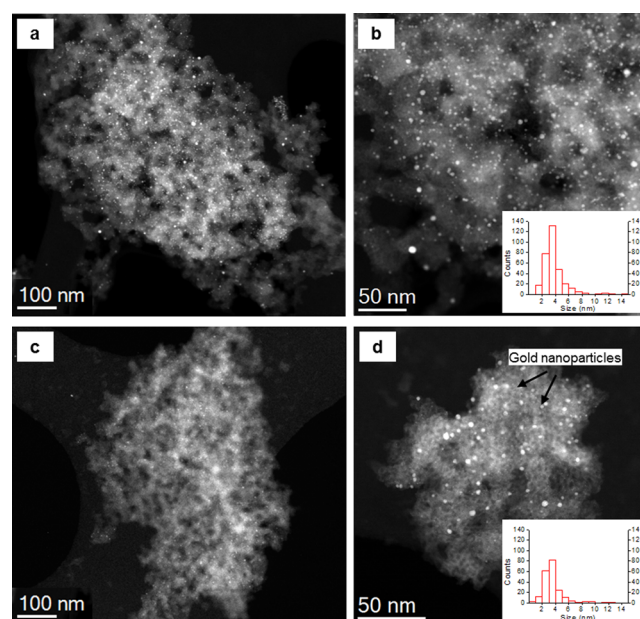


Figure 1. C_s -corrected STEM-HAADF images and gold particle size distribution of the (a, b) uncalcined and (c, d) calcined at 800 °C Au/Ti8/UVM-7 catalysts. Particle size distributions are shown as insets for (b) uncalcined and (d) calcined samples.

spherical aberration (C_s) corrected scanning transmission electron microscopy high-angle annular field (STEM-HAADF) images of the uncalcined Au/Ti8/UVM-7 catalyst. Similar images of the sample after calcination at 800 °C for 4 h (Figure 1c,d) confirm that the gold nanoparticles are thermally stable, as the high-temperature treatment does not result in sintering, preserving their original size and maintaining a homogeneous distribution over the mesoporous support. The uncalcined sample shows some small 1 nm gold nanoparticles and has a unimodal particle size distribution, with most particles in the 1–6 nm range. The predominant particle size of

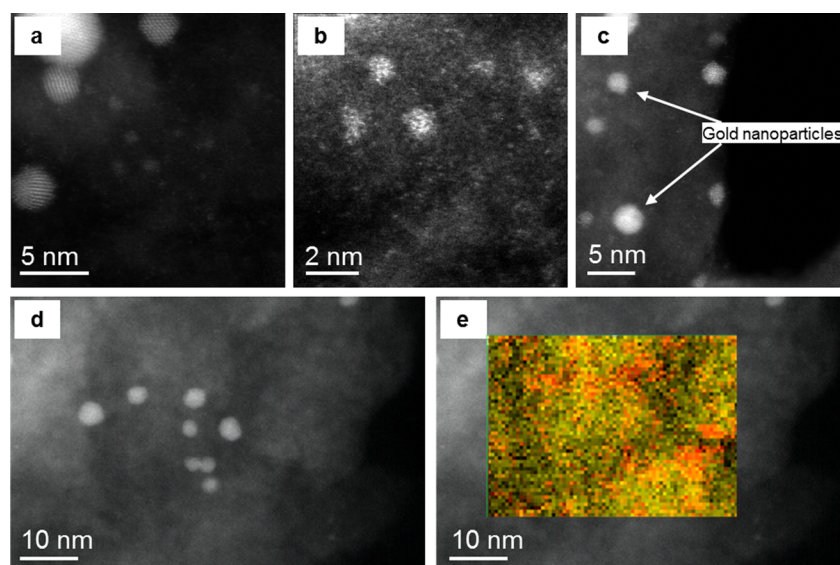


Figure 2. C_s -corrected STEM-HAADF images of Au/Ti8/UVM-7. (a–c) High-magnification images where gold nanoparticles are identified. (d) C_s -corrected STEM-HAADF image where an EELS spectrum-image is recorded. (e) Ti- $L_{3,2}$ (red) and O-K (yellow) maps superimposed on the experimental STEM image.

Table 2. Textural Characterizations of UVM-7 Materials Loaded with Titania and Gold/Titania

catalyst	surface area (m^2/g)	intrapart pore size ^a (nm)	intrapart pore volume (cm^3/g)	interpart pore size (nm)	interpart pore volume (cm^3/g)
UVM-7	1136	2.87	1.01	29.0	1.20
Ti8/UVM-7	931	2.81	0.79	25.5	0.88
Au/Ti8/UVM-7	845	2.82	0.72	36.8	1.30
Au/Ti8/UVM-7 800	245	1.30 /2.75 ^a	0.14	27.2	0.68

^aIntraparticle pore size determined by the application of the DFT model.

the uncalcined sample is 3.73 ± 1.60 nm, which surprisingly does not dramatically increase after calcination at 800°C (3.50 ± 1.57 nm). XRD is also used to probe the dispersion and stability of the gold nanoparticles (Figure S3). Unchanged diffraction peaks (of very low intensity) from gold species are observed before and after calcination at 800°C (even for the samples after the catalytic reaction), consistent with the TEM, indicating that gold species remain well dispersed on the support even after high-temperature treatment (Figure 1d).

The exceptional catalytic performance of these materials also can be related to the way in which titanium is present on the UVM-7 support. For the uncalcined sample, different spectroscopic techniques support the formation of species including Ti–O–Si bonds between Ti-oligomers (produced after degradation of the $\text{TiO}(\text{acac})_2$ precursor at 300°C) and the silica surface, where a certain proportion of Ti^{4+} occupies a tetrahedral coordination site similar to Si in SiO_2 (Figure S4). In fact, a slight increase of the binding energy of both Ti $2p_{3/2}$ and the second component of O 1s compared to pure TiO_2 is observed, consistent with diffusion of Ti species into the silica wall^{27,28} (Table S3). This shift is also accompanied by an increase of the oxidation potential of the Ti(IV) cations, which may enhance the oxygen mobility at the gold/Ti–O–Si interface, thus enhancing the CO oxidation activity at low temperature²⁹ (Table 1). Accordingly, the existence of a regular and homogeneous dispersion of titanium for the uncalcined sample is also confirmed by STEM images in Figure 2. This extremely regular dispersion of Ti species on the silica surface also favors the subsequent homogeneous

distribution of AuCl_4^- complexes and finally of gold nanoparticles achieved during the deposition-precipitation step.

Upon calcination at 800°C , the catalyst still presents very high activity, although a certain loss of activity is clearly observed when compared to uncalcined materials. This loss of activity can be linked to different factors. With respect to gold, although the nanoparticle size is preserved, it cannot be discounted that there could be a decrease of activity due to a change of the gold surface oxidation state.^{30,31} Accordingly, the oxidation state of gold on the surface of the nanoparticles is investigated using XPS. The uncalcined catalyst has some cationic gold, ($\text{Au}^{3+}/\text{Au}^0 = 0.24$), whereas only metallic gold is present after heat treatment at 800°C (Figure S5 and Table S4). More importantly, the calcination probably induces changes to the Ti species, although these are more complex, and may not directly be related with the catalytic activity. First, it is observed that Ti species only remains partly as Ti–O–Si species, supported by XPS results (Figure S4 and Table S3), and corroborated by ^{29}Si NMR (Figure S6). The ^{29}Si NMR spectrum of the Ti8/UVM-7 support shows a 5% increase of the signals at ca. -100 and -93 ppm (corresponding to Si environments with 1 and 2 atoms of Ti as neighbors, respectively: Si (3Si, 1Ti) and Si (2Si, 2Ti))³² and a decrease in the Q^4 signal (at ca. -110 ppm) when compared with the spectrum of the UVM-7 silica pure support and calcined at the same temperature, in which some Si–OH groups are still preserved (signal at ca. -110 ppm, Figure S6 and Table S5). These data allow us to determine that an additional 38% of titanium atoms are incorporated into the UVM-7 silica wall (by

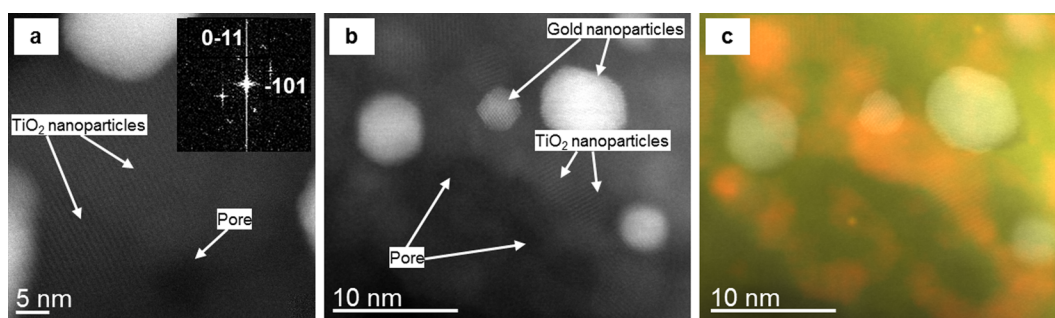


Figure 3. C_s -corrected STEM-HAADF images of Au/Ti8/UVM-7 800. (a) High-magnification image where the TiO_2 nanoparticles are identified together with the Au nanoparticles. The FFT of the TiO_2 phase is shown as an inset. (b) C_s -corrected STEM-HAADF image where an EELS spectrum-image is recorded. (c) $\text{Ti-L}_{3,2}$ (red) and O-K (yellow) maps superimposed on the HRSTEM-HAADF image.

diffusion at 800 °C) and the remaining Ti (62%) must initiate a process of nucleation and growth of TiO_2 domains.

It is worth mentioning that the modification of the architecture/mesostructure of the siliceous support could be a key parameter upon calcination, leading to ultrastable gold nanoparticles. Thus, although calcination results in an expected reduction of both surface area and pore volume, when compared with the uncalcined material, the highly active Au/Ti8/UVM-7 800 catalyst still preserves a relatively high specific BET surface area of 245 m^2/g and a total pore volume of 0.82 cm^3/g , which includes 0.14 cm^3/g associated with the internal porosity (Table 2; Figure S7 and Table S6). Applying a density functional theory (DFT) model also allows us to detect the existence of some microporosity in the calcined sample. This microporosity along with a partial preservation of the original mesoporosity seems to be improved by the presence of TiO_2 and Au (Figure S8), because the UVM-7 support completely collapses after calcination at 800 °C. Thus, values of 151 m^2/g and 0.14 cm^3/g can be estimated for the intraparticle porosity (excluding the textural component) in the case of sample Au/Ti8/UVM-7 800. The generation/preservation of this micro-mesoporosity, which must be understood as the result of a partial collapse of the original mesostructure, is most likely the key to explaining both the high catalytic activity (directly related to resistance to sintering of the particles of Au) and the loss of activity compared to the uncalcined catalyst due to a certain loss of accessible active sites that become trapped.

Therefore, it can be assumed that the TiO_2 crystallites covering the internal porous surface of the support could have an important role in enhancing the thermal stability of the UVM-7 mesostructure, acting as a scaffold of the support, as suggested by the surface area increase with the Ti content of the Au/Ti15/UVM-7 800 (Table S6) and the total collapse of the Au/UVM-7 800 structure (Figure S9). Accordingly, it was observed that the high BET surface area and bimodal porosity of the materials was preserved for titania loadings up to ca. 15 wt % (Ti15/UVM-7 sample) (Table S7). For higher titania loading (40 wt %), a dramatic decrease of these textural parameters occurred, which indicates a significant mesopore blocking (affecting both the gold deposition and the CO accessibility), with the subsequent loss of catalytic activity. Upon calcination, TiO_2 partially agglomerates in the form of small TiO_2 nanodomains with sizes just slightly larger than that of the gold nanoparticles (Figure 3; Figure S4 and Table S3). The absence of titania diffraction in the XRD is further evidence for the small size of the TiO_2 domains (Figure S3). Accordingly, microscopy data show (Figure 3a) the high-resolution images of the gold and the TiO_2 nanoparticles. The

titania FFT diffractograms can be indexed assuming I41/amd symmetry corresponding to anatase and lattice parameters $a = 3.78 \text{ \AA}$ and $b = 9.51 \text{ \AA}$ (Figure 3b). Laser Raman spectroscopy (Figure S10) also confirms the presence of titania with anatase as the predominant crystalline phase for the Au/Ti8/UVM-7 800 sample.³³ The UVM-7 support seemed to stabilize the anatase phase, although a retarding effect over the phase transition from anatase to rutile due to the presence of gold nanoparticles could not be ruled out. Although this agglomeration of the Ti species seems to be detrimental for the catalyst performance,²⁹ as also suggested by the loss of activity with the increasing Ti content, the nanocrystalline nature of the anatase domains also seemed to induce a strong interfacial anchoring effect between TiO_2 and the gold nanoparticles, negating their sintering after high-temperature calcination.³⁴ Indeed, for gold supported directly on the mesoporous UVM-7 support, the gold nanoparticles readily agglomerate and, for the calcined sample, large gold nanoparticles together with small nanoparticles are formed (Figure S9), and a total structure collapse is evident. The presence of both small and large nanoparticles is in accordance with Qian et al., who reported the coexistence of both small and large sizes of gold nanoparticles for Au/ SiO_2 catalysts calcined at high temperatures,²⁶ proposing that small gold nanoparticles are formed by an evaporation–deposition mechanism. Accordingly, gold nanoparticles are observed close to the titania nanodomains only on the UVM-7 surface (Figure 3), which is corroborated by the combination of STEM-HAADF images and chemical mapping based on electron energy loss spectroscopy measurements (Figure 3b,c). The TiO_2 domains have dual roles, as a scaffold,³⁵ preventing the complete mesostructure collapse, and as an anchoring island to avoid gold sintering. Hence, the exceptional thermal stability of gold nanoparticles in Au/Ti8/UVM-7 could be viewed as the combined result of a strong anchoring of gold on titania nanoparticles homogeneously dispersed on the preserved UVM-7 internal surface and the confinement effect that is provided by the silica mesostructure and the anatase nanocrystals.

We have studied UVM-7 supported gold catalysts modified by other metal oxides by using this simple preparation method to see if the highly active and stable gold nanoparticles are specific to titania modification. After an optimization procedure to select the proper metal oxide loadings, gold nanoparticles are deposited onto $\text{ZrO}_2/\text{UVM-7}$ and $\text{CeO}_2\text{-ZrO}_2/\text{UVM-7}$ supports. It should be noted that regardless of the metal oxide nanodomains included inside the mesopores, a preferred interaction of the gold nanoparticles with these metal oxides

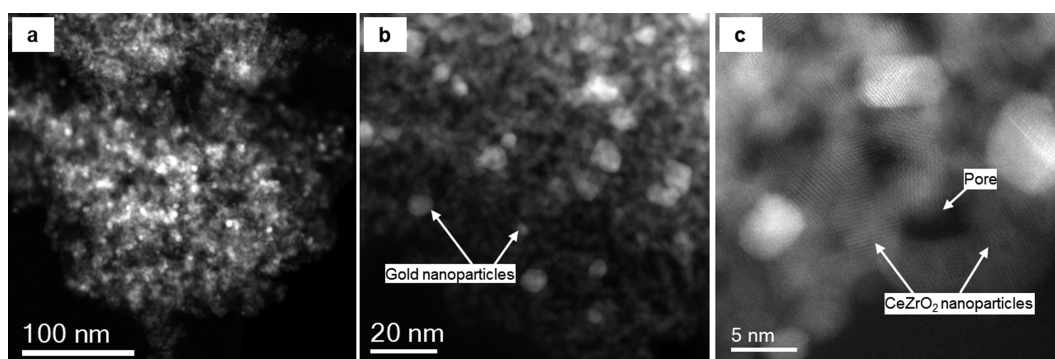


Figure 4. C_s -corrected STEM-HAADF images of Au/CeO₂-ZrO₂/UVM-7 800 at (a) low magnification observing a homogeneous distribution of gold, (b) medium magnification image, and (c) high magnification observing *fcc* Au nanoparticles and some crystalline CeZrO₂ domains.

is observed. This is again a key factor favoring the presence of highly dispersed small gold nanoparticles. Additionally, as observed for TiO₂/UVM-7 supports, these metal oxide nanodomains also act as scaffolds for the UVM-7 support, preventing silica from complete collapse and preserving a certain porosity to favor the diffusion of CO to the active sites, and as anchoring islands for gold nanoparticles, providing stability against sintering after calcination at 800 °C, resulting in highly thermally stable gold nanoparticles (Figure 4 and Figure S11).

As shown in Table 1, these gold catalysts calcined at 800 °C are also very active for the model CO oxidation reaction at 20 °C. The catalytic activity is lower for both zirconia and cerium-modified zirconia than for titania, but Au/ZrO₂/UVM-7 800 still has a productivity of 0.0026 mol CO/(g_{cat}·h) and Au/CeO₂-ZrO₂/UVM-7 800 is more active, achieving a productivity of 0.0061 mol CO/(g_{cat}·h) (Table S8). The addition of zirconia is known to increase the thermal stability of CeO₂,³⁶ and this is consistent with our observations. Importantly, although some differences might be expected in the final oxides depending on the type of precursor used, our preliminary results with zirconium and cerium oxides indicate that there are no differences in the role played by the oxidic domains (TiO₂, ZrO₂, CeO₂-ZrO₂) from the structural/morphological point of view: they act as inorganic anchors for the gold particles and as scaffolds to prevent a massive mesostructure collapse. However, we note that the gold nanoparticles anchored on ZrO₂ and CeO₂-ZrO₂ have slightly higher sizes than those observed on anatase domains (Table 1). These differences together with the intrinsic characteristics of each catalytic system could be responsible for the different catalytic activities observed. Thus, it appears that the beneficial stabilization effect is not restricted to titania with the UVM-7 support, as similar beneficial effects are also observed with zirconia and ceria-zirconia, which highlights the versatility of these nanostructured materials to be implemented into new high-temperature processes.

We are able to illustrate the exceptional thermal stability of gold nanoparticles on metal oxide modified UVM-7 by employing the catalyst for several high-temperature applications. We have exemplified this using CO emission control during the cold-start process of an engine. The evolution of CO concentration of a stream of 1.6% v/v CO, 0.01% v/v propene, 0.0087% v/v toluene, and 1% v/v O₂ by increasing the reactor temperature from 30 to 600 °C at 50 °C/min over the Au/Ti8/UVM-7 800 shows 100% CO removal in the presence of 10% v/v H₂O after 10 consecutive cycles at a space velocity of 200000 h⁻¹ (Figure 5). There is no appreciable gold

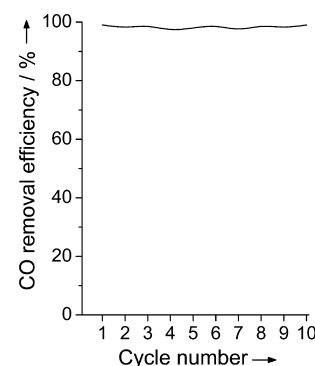


Figure 5. CO removal efficiency under simulated cold-start conditions of Au/Ti8/UVM-7 800 catalyst. Conditions: 1.6% v/v CO, 0.01% v/v propene, 0.0087% v/v toluene, 1% v/v oxygen, 10% v/v water and Ar balance, GHSV = 200000 h⁻¹. Temperature is increased from 30 to 600 °C at 50 °C/min.

nanoparticle sintering after use (2.3 ± 0.6 nm, Figure 6). Panels a and b of Figure 6 confirm the homogeneous nanoparticle dispersion after reaction preserving a diameter below 5 nm and, as already described, the chemical analysis corroborates the affinity between the position of the TiO₂ domains and the Au nanoparticles, preventing gold sintering under severe conditions.

This catalyst is also tested as a three-way catalyst under a reaction mixture of 1% v/v CO, 0.1% v/v propane, 0.03% v/v NO, 8% v/v O₂, 6% v/v CO₂, and 8% v/v H₂O, space velocity of 40000 h⁻¹, and at a reaction temperature of 500 °C, showing remarkable hydrothermal stability after three consecutive cycles (Figure S12). The stability and activity were also validated using methane catalytic oxidation of 1% v/v CH₄ in air by increasing the reactor temperature from 300 to 800 °C at a space velocity of 60000 h⁻¹. Stable catalyst performance is maintained for at least five consecutive cycles (Figure 7).

CONCLUSIONS

Gold nanoparticles with exceptional thermal stability have been synthesized in an easy and reproducible method, following a wet impregnation procedure of UVM-7 porous silica with titanium(IV) oxyacetylacetonate followed by a conventional deposition–precipitation approach. As a model reaction, CO oxidation was initially selected to evaluate the performance of Au/TiO₂/UVM-7 catalysts. An extraordinary stability and excellent catalytic activity after high-temperature treatment were achieved, which is in agreement with the small size and

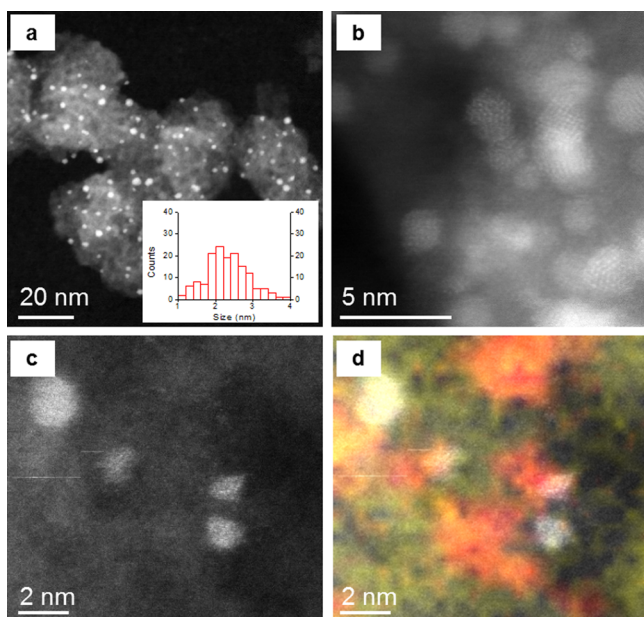


Figure 6. C_s -corrected STEM-HAADF images of the Au/Ti8/UVM-7 800 catalyst after 10 consecutive cold-start tests: (a) low-magnification image showing the nanoparticle distribution as inset; (b) high-magnification image; (c) C_s -corrected STEM-HAADF image where an EELS spectrum image is recorded; (d) Ti- $L_{3,2}$ (red) and O-K (yellow) maps superimposed on the HRSTEM-HAADF image.

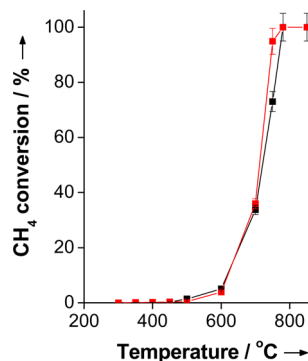


Figure 7. Methane conversion versus reactor temperature of Au/Ti8/UVM-7 800 catalyst in methane catalytic oxidation. Black line and red line correspond to the first and fifth cycles, respectively. Conditions: 1% v/v CH_4 in air, GHSV = 60000 h^{-1} .

high dispersion of gold nanoparticles. The open architecture of the UVM-7 silica combined with the presence of anatase nanocrystals inside the pore system leads to the establishment of strong interfacial interactions with Au nanoparticles, which are responsible for stabilizing Au nanoparticles at temperatures as high as 800 °C. The optimum performance of the Au/Ti8/UVM-7 sample was linked to an optimal interplay between the presence of Ti as amorphous titanium silicate, the presence of small gold nanoparticles with high sintering resistivity (both beneficial for the catalytic activity), and TiO_2 nanocrystallites (beneficial for the stabilization of both the UVM-7 porosity and the gold nanoparticles). Moreover, the antisintering ability of gold nanoparticles was demonstrated by several high-temperature catalytic applications. Finally, the extension of titania modification to other metal oxides makes these catalysts broadly applicable for a variety of catalytic applications, such as catalytic combustion, steam reforming, or automobile exhaust

control, especially for their application in novel hybrid and micro hybrid cars.

■ ASSOCIATED CONTENT

§ Supporting Information

The following file is available free of charge on the ACS Publications website at DOI: 10.1021/cs501741u.

Results of XRD, N_2 sorption, Raman, XPS, ^{29}Si MAS NMR, TEM, and catalytic performance (PDF)

■ AUTHOR INFORMATION

Corresponding Authors

*(B.S.) E-mail: benjamin.solsona@uv.es.

*(T.G.) E-mail: tomas@icb.csic.es.

Notes

The authors declare no competing financial interest.

■ ACKNOWLEDGMENTS

This research was supported by the Spanish Ministerio de Economía y Competitividad and European Feder Funds (MAT2012-38429-C04-03, CTQ2012-37984-C02-01, CTQ2012-37925-C03-2). The TEM measurements were performed in the Laboratorio de Microscopias Avanzadas (LMA) at the Instituto de Nanociencia de Aragón (INA), Universidad de Zaragoza (Spain), and received funding from the European Union Seventh Framework Program under Grant Agreement 312483-ESTEEM2 (Integrated Infrastructure Initiative-I3). B.P. thanks the Ministry of Education for the FPU grant (AP2009-3544). A.M. thanks the Ministry of Economía y Competitividad for the FPI grant (BES2009-040029).

■ REFERENCES

- (1) Bond, G. C.; Thompson, D. T. *Catal. Rev. Sci. Eng.* **1999**, *41*, 319–388.
- (2) Rodriguez, J. A.; Viñes, F.; Illas, F.; Liu, P.; Takahashi, Y.; Nakamura, K. *J. Chem. Phys.* **2007**, *127*, 211102.
- (3) Haruta, M. *Gold Bull.* **2004**, *37*, 27–36.
- (4) Guzman, J.; Carrettin, S.; Corma, A. *J. Am. Chem. Soc.* **2005**, *127*, 3286–3287.
- (5) Haruta, M.; Tsubota, S.; Kobayashi, T.; Kageyama, H.; Genet, M. J.; Delmon, B. *J. Catal.* **1993**, *144*, 175–192.
- (6) Haruta, M.; Daté, M. *Appl. Catal., A* **2001**, *222*, 427–437.
- (7) Lee, L.; Joo, J. B.; Yin, Y.; Zaera, F. *Angew. Chem., Int. Ed.* **2011**, *50*, 10208–10211.
- (8) Campbell, C. T.; Parker, S. C.; Starr, D. E. *Science* **2002**, *198*, 811–814.
- (9) Joo, S. H.; Park, J. Y.; Tsung, C.-K.; Yamada, Y.; Yang, P.; Somorjai, G. A. *Nat. Mater.* **2009**, *8*, 126–131.
- (10) Narayanan, R.; El-Sayed, M. A. *J. Am. Chem. Soc.* **2003**, *125*, 8340–8347.
- (11) Zarur, A. J.; Ying, J. Y. *Nature* **2000**, *403*, 65–67.
- (12) Gandhi, H. S.; Graham, G. W.; McCabe, R. W. *J. Catal.* **2003**, *216*, 433–442.
- (13) Zhu, H.-G.; Ma, Z.; Overbury, S. H.; Dai, S. *Catal. Lett.* **2007**, *116*, 129–135.
- (14) Arnal, P. M.; Comotti, M.; Schüth, F. *Angew. Chem., Int. Ed.* **2006**, *45*, 8224–8227.
- (15) Chen, C.; Shi, M.; Cargnello, M.; Fornasiero, P.; Murray, C. B.; Gorte, R. J. *Catal. Lett.* **2014**, *144*, 1939–1945.
- (16) Zhang, T.; Zhao, H.; He, S.; Liu, K.; Liu, H.; Yin, Y.; Gao, C. *ACS Nano* **2014**, *8*, 7297–7304.
- (17) Zhao, K. F.; Qiao, A.; Wang, J.; Zhang, Y.; Zhang, T. *Chem. Commun.* **2011**, *47*, 1779–1781.
- (18) Wang, J.; Lu, A.-H.; Li, M.; Zhang, W.; Chen, Y.-S.; Tian, D.-X.; Li, W.-C. *ACS Nano* **2013**, *7*, 4902–4910.

- (19) Corti, C. W.; Holliday, R. J.; Thompson, D. T. *Gold Bull.* **2002**, *35*, 111–117.
- (20) El Haskouri, J.; Ortiz de Zárate, D.; Guillem, C.; Latorre, J.; Caldés, M.; Beltrán, A.; Beltrán, D.; Descalzo, A. B.; Rodríguez-López, G.; Martínez-Máñez, R.; Marcos, M. D.; Amorós, P. *Chem. Commun.* **2002**, 330–331.
- (21) El Haskouri, J.; Morales, J. M.; Ortiz de Zárate, D.; Fernández, L.; Latorre, J.; Guillem, C.; Beltrán, A.; Beltrán, D.; Amorós, P. *Inorg. Chem.* **2008**, *47*, 8267–8277.
- (22) Pérez-Cabero, M.; Hungría, A. B.; Morales, J. M.; Tortajada, M.; Ramón, D.; Moragues, A.; El Haskouri, J.; Beltrán, A.; Beltrán, D.; Amorós, P. *J. Nanopart. Res.* **2012**, *14*, 1045.
- (23) Narkhede, V. S.; De Toni, A.; Narkhede, V. V.; Guraya, M.; Niemantsverdriet, J. W.; van den Berg, M. W. E.; Grünert, W.; Gies, H. *Microporous Mesoporous Mater.* **2009**, *118*, 52–60.
- (24) Jeanguillaume, C.; Colliex, C. *Ultramicroscopy* **1989**, *281*, 252–257.
- (25) Arenal, R.; de la Peña, F.; Stéphan, O.; Walls, M.; Tencé, M.; Loiseau, A.; Colliex, C. *Ultramicroscopy* **2008**, *109*, 32–38.
- (26) Qian, K.; Jiang, Z.; Huang, W. *J. Mol. Catal. A: Chem.* **2007**, *264*, 26–32.
- (27) Castillo, R.; Koch, B.; Ruiz, P.; Delomn, B. *J. Catal.* **1996**, *161*, 524–529.
- (28) Santacesaria, E.; Cozzolino, M.; Di Serio, M.; Venezia, A. M.; Tesser, R. *Appl. Catal., A* **2004**, *270*, 177–192.
- (29) Venezia, A. M.; Liotta, F. L.; Pantaleo, G.; Beck, A.; Horváth, A.; Gestzi, O.; Kocsonya, A.; Guzzi, L. *Appl. Catal., A* **2006**, *310*, 114–121.
- (30) Hutchings, G. J.; Hall, M. S.; Carley, A. F.; Landon, F.; Solsona, B. E.; Kiely, C. J.; Herzing, A.; Makkee, M.; Moulijn, J. A.; Overweg, A.; Fierro-Gonzalez, J. C.; Guzman, J.; Gates, B. C. *J. Catal.* **2006**, *242*, 71–81.
- (31) Guzman, J.; Gates, B. C. *J. Am. Chem. Soc.* **2004**, *126*, 2672–2673.
- (32) Labouriau, A.; Higley, T. J.; Earl, W. L. *J. Phys. Chem. B* **1988**, *102*, 2897–2904.
- (33) Kirchhoff, M.; Spetch, U.; Vesper, G. *Nanotechnology* **2005**, *16*, S401–S408.
- (34) Debeila, M. A.; Raphulu, M. C.; Mokoena, M.; Avalos, M.; Petranovskii, V.; Coville, N. J.; Scurrrell, M. S. *Mater. Sci. Eng., A* **2005**, *396*, 61–69.
- (35) Knowles, J. A.; Hudson, M. J. *J. Chem. Soc., Chem Commun.* **1995**, 2083–2084.
- (36) Murrell, L. L.; Tauster, S. J. In *Studies in Surface Science and Catalysis: Catalysis and Automotive Pollution Control II*; Elsevier: Amsterdam, The Netherlands, 1991; Vol. 71, p 547.